Correlation hard gap in antidot graphene

Jie Pan,[1,*] Sheng-Shiuan Yeh,[2,3,*] Haijing Zhang,[1,†] David G. Rees,[2,‡] Ting Zhang,[1] Bing Zhang,[1] Juhn-Jong Lin,[2,4,§] and Ping Sheng[1,‖]

[1]*Department of Physics, HKUST, Clear Water Bay, Kowloon, Hong Kong, China*

[2]*Institute of Physics and Center for Emergent Functional Matter Science, National Yang Ming Chiao Tung University, Hsinchu 30010, Taiwan*

[3]*International College of Semiconductor Technology, National Yang Ming Chiao Tung University, Hsinchu 30010, Taiwan*

[4]*Department of Electrophysics, National Yang Ming Chiao Tung University, Hsinchu 30010, Taiwan*

(Received 23 November 2020; revised 23 May 2021; accepted 25 May 2021; published 8 June 2021)

We have measured low-temperature variation of resistance and nonlinear current-voltage behavior in antidot graphene in the vicinity of the charge neutrality point. The data are found to be consistent with the manifestations of a variable-range hopping electronic density of states (DOS) with a small hard gap of ~ 1 meV around the Fermi level, in conjunction with a parallel tunneling conduction channel that exists at the center of the gap. The hard gap is confirmed by the appearance of a low-conductive plateau at low-bias electric field, whereas the parallel tunneling conduction channel, with temperature-independent conductance, is manifest through the nonlinear electric field variation. Unified good agreement between the temperature and electric field dependencies of conductance, for both channels, is obtained with the predictions of a proposed DOS model. An increase in the gap size with applied magnetic field is observed.

DOI: 10.1103/PhysRevB.103.235114

I. INTRODUCTION

Graphene is gapless with a linear dispersion relation at the Dirac point [1–5]. To open a gap, one can either break the inversion symmetry by aligning graphene on h-BN [6–9] or by etching graphene into nanoribbons [10–14] or antidot graphene [15–26]. From tight-binding simulations, it is known that, within the band structure gap (which is ~ 20 meV in our case) of the antidot graphene, there can be many localized states arising from those atoms at the edges of the holes [18]. These defect-localized states give rise to the two-dimensional (2D) variable-range hopping (VRH) conductance G characterized by the $\ln G \sim -T^{-1/3}$ behavior [21,22], indicating a constant density of states (DOS) for such defect states. Here, T denotes temperature. In this paper, however, we find in two similarly made samples that, at the charge neutrality point (CNP), both the temperature variation of G, <14 K for one sample and <30 K for the other, as well as the low-temperature nonlinear current-voltage (I-V) behavior are consistent with the opening of a small hard gap around the Fermi level. We attribute this hard gap to the electronic correlation effect. We further show that there is a low DOS around the Fermi level, manifest as a parallel conduction channel that exhibits temperature-independent conductance, which exhibits 2D Anderson-localized states with micron-scale localization length that was also previously observed [22].

The two-conduction channel behavior, with a hard gap for the VRH states and a low density of Anderson-localized states, represents the main results of this paper. We attribute the large localization length of the Anderson-localized states to the suppression of the inelastic scatterings. This is in sharp contrast to the VRH states, whose localization length (<100 nm) is much smaller because of the cutoff by inelastic (phonon-assisted) scatterings that are an inherent part of the VRH mechanism. We speculate the reason for the existence of the low DOS Anderson-localized states to be the coincidence of the Fermi level with the CNP, where an equal number of electrons and holes may imply a correlation energy ground state. In fact, an estimate of the excitation energy of the charge carrier from such a proposed model ground state is quantitatively consistent with the experimentally observed nonlinear I-V behavior; hence, it can offer an alternative interpretation to the nonlinear electrical behavior. Despite lacking an overall first-principles theoretical framework for all observed phenomena, our proposed DOS model is nevertheless noted to offer a unified agreement with the experimental temperature and electrical field variations of conductance, as shown below. Hence, this paper may be regarded as an opening to further investigations.

The antidot lattice has a significant impact on the electron-electron interactions, i.e., correlation effect, in a graphene system. The relative importance of the correlation effect can be assessed by the magnitude of the ratio r_S between the Coulomb interaction energy and the kinetic energy of the electrons. For pristine graphene on SiO_2 substrate, $r_S = 0.9$, independent of the carrier density [4,5]. For antidot graphene,

*These authors contributed equally to this work.

†Present address: Max-Planck-Institute for Chemical Physics of Solids, Nöthnitzer Straße 40, Dresden, Germany.

‡Present address: Cryogenic Ltd, 6 Acton Park Estate, The Vale, London W3 7QE, United Kingdom.

§jjlin@mail.nctu.edu.tw

‖Corresponding author: sheng@ust.hk

the dispersion relation is hyperbolic, and r_S at CNP is estimated to be 2.4 (see the Supplemental Material (SM) [27] for details). We attribute the appearance of an effective correlation hard gap, on the order of 1 meV, in the VRH DOS to this enhanced Coulomb correlations. We note that this hard gap is different from the previously reported Coulomb quasigap [20–22], where the DOS is zero only at the Fermi level E_F, while finite at $E \neq E_F$. The correlation hard gap has been theoretically proposed [28]. By stabilizing the ground state to electronic polaron excitations, it was estimated that the magnitude of the correlation hard gap should be $\sim\frac{1}{5}$ of the Coulomb quasigap. In our sample, it can be simply estimated as $E_{\text{hard}} = E_{\text{quasi}}/5 \sim 1.4$ meV, in reasonable quantitative agreement with our observed value, where $E_{\text{quasi}} = g_0[e^2/(4\pi\varepsilon_0\kappa_{\text{eff}})]^2 \sim 7$ meV is the Coulomb quasigap energy. Here, g_0 is the DOS in our sample, which is $\sim 10^{10}/(\text{meV cm}^2)$ (see below), and κ_{eff} is the effective dielectric constant under screening in the long wavelength limit [5,29], taken to be 5.5.

The correlation hard gaps have been experimentally observed in many other material systems such as magnetic materials [30,31], amorphous In/InO_x films [32], and ultrathin beryllium [33]. Such a hard gap size varies from 0.04 to 30 meV in these different materials. The hard gap was also found to be suppressed [30], almost unchanged [32], and enhanced [33] upon applying a magnetic field. There were also correlation hard gaps reported in bilayer and twist double bilayer graphene systems [34–36], with different magnetic field dependencies attributed to either spin polarized or spin unpolarized ground states [35,36]. These diverse observations reflect the complexity of the correlation effect in various disordered electronic systems.

In our antidot graphene samples, the effective gap size was found to increase monotonically with applied magnetic field (see below). The existence of the hard gap was evidenced by both the thermal activation behavior of zero-bias $G(T)$ and a strong nonlinear I-V phenomenon at 100 mK. The $\ln G \sim -T^{-1/3}$ behavior, the transition to the thermal activation behavior, plus the nonlinear I-V phenomenon, were found to be explainable on a unified basis by a DOS model that exhibits a correlation hard gap, plus a small bump in DOS, around the Fermi level. In addition, we find that, in the low-temperature tunneling conductance, the Anderson-localized states have localization length on the order of micrometers. Such a large localization length is consistent with previously reported 2D Anderson-localized states [22] in antidot graphene. Furthermore, we present tight-binding calculations that show the states in the band structure gap can have a localized region around the edge of the antidot holes, attendant with a power-law tail. The latter is proposed to be the source of the 2D Anderson-localized states.

In what follows, we introduce the experimental method in Sec. II, followed by the presentation of experimental results in Sec. III. We examine the temperature dependence of CNP conductance to find a linear relation between $\ln G$ and T^{-1}, indicating the existence of a correlation gap at the Fermi level. In Sec. IV, we propose a DOS model with a hard gap in the DOS of the VRH states; we show that the measured temperature variation, from 2 to 100 K, can be well explained within our DOS model. In Sec. V, we focus on the Anderson-localized states, which dominate the electronic transport at ultralow temperatures (<1 K). By exploring the electric field dependence, we find the localization length of the Anderson-localized states to be quite large (~ 1 μm), which is consistent with the results reported previously. To reconcile the existence of both the VRH states and the Anderson-localized states, we summarize the tight-binding simulation results in Sec. VI and propose that both the VRH and the Anderson-localized states originate from the quasiflat band states in antidot graphene. In addition to the consistency between the VRH states density and the estimated quasiflat band states density, these states' wave functions are found to exhibit an extended power-law decaying tail, which can be the origin of the Anderson-localized states. We conclude by summarizing the important points of this paper in Sec. VII.

II. EXPERIMENTAL METHOD

The graphene flake was first exfoliated onto Si substrates capped with 285 nm SiO_2. The antidot lattice and Hall bar geometry structure were patterned by e-beam lithography, followed by oxygen plasma etching. The width of the sample was 0.5 μm, and electrode separation was 2 μm, as shown in Fig. 1(a). The antidot lattice has a triangular lattice structure with a lattice constant of 150 nm and hole diameter of 100 nm, shown by the scanning electron microscope image in Fig. 1(a). Subsequently, 5 nm of Ti and 70 nm of Au were deposited to form the electrodes.

The electrical-transport measurements were carried out on a BlueFors LD-400 dilution refrigerator with room- and low-temperature low-pass filters. The insulation resistances of the measurement wires were ~ 10 GΩ, which were limited by the leakage resistances of the capacitors used in the low-pass filters. We used the sourcemeter Keithley 6430 with a preamplifier to apply a DC bias voltage (denoted as V_{sd}) as well as to measure the current I. The voltage dropped across the sample (denoted as V) was amplified by a SR560 preamplifier (Stanford Research Systems) and measured by a Keithley 182 voltmeter. The gate voltage V_G was applied by a Keithley 2635 sourcemeter in series with a 1 MΩ resistor. We have carried out both 2-probe and 4-probe measurements, with consistent results. That implied the contact resistance to be negligible. The measured resistance was also found to scale with the corresponding electrode separations, indicating a high degree of uniformity for our antidot graphene samples.

III. CORRELATION HARD GAP IN ANTIDOT GRAPHENE

We have measured two antidot graphene samples and found both to exhibit similar behavior. The I-V curves were measured at 100 mK under zero magnetic field. A strong nonlinear behavior was seen in the vicinity of the CNP with a flat plateau, i.e., a very low-conductance region, implying the existence of a gap. A plot of dI/dV as a function of both the bias voltage V_{sd} and the gate voltage V_G is shown in Fig. 1(b). It is seen that a gap appeared around the CNP $V_G = 2.8$ V, with a 10 mV "width" of the plateau region. However, the width of the measured plateau is not equivalent to the gap size. Instead, it indicates that there is a critical electric field given by 5 mV/10 μm = 0.5 mV/μm (where 10 μm is the sample length between the source and drain electrodes) that can help

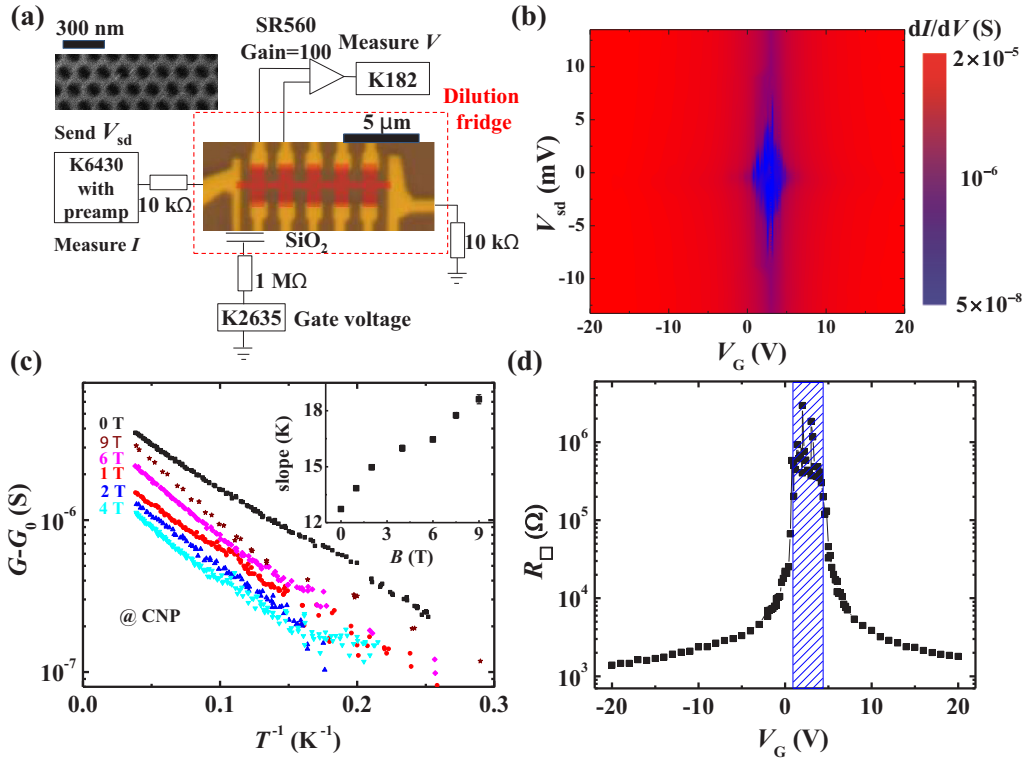

FIG. 1. Measurement setup and hard gap in antidot graphene. (a) Experimental setup with a microscope image of antidot graphene sample indicated by the red region. The black scale bar denotes 5 μm. The scanning electron microscopic image of the antidot lattice is shown in the top left corner. The magnetic field was applied perpendicular to the sample. (b) A two-dimensional (2D) map of dI/dV as a function of the gate voltage and the source drain bias voltage V_{sd}. An insulating region (blue color) was observed at $V_G \sim 2.8$ V, which disappears as V_G deviates away from the charge neutrality point (CNP). (c) Arrhenius plots of conductance $G - G_0$ as a function of $1/T$. Conductance is measured at CNP under various magnetic fields. The conductance shows good linear relation with different slopes at different magnetic fields, implying a different thermal activation gap. Inset summarizes fitted slopes as a function of the applied magnetic fields. (d) Derived sheet resistance as a function of the gate voltage. Data in (b) and (d) were measured at 100 mK under zero magnetic field.

the carriers to overcome the gap. As V_G is tuned away from the CNP, the size of the correlation gap decreases, which is clearly evidenced by the narrowing width of the low dI/dV plateau in Fig. 1(b).

To estimate the gap size, we measure the temperature dependence of the zero-bias conductance at the CNP. In the Arrhenius plots in Fig. 1(c), we summarize the subtracted conductance $G - G_0$ (where G_0 is the temperature-independent conductance at low temperatures [shown in Fig. 2(b)] that represents the parallel channel of tunneling conduction) as a function of T^{-1} (detailed discussion about conductance as a function of temperature [37] is included in the SM [27]); good linear relations were observed for different magnetic fields. Their slopes are seen to increase with the applied magnetic field, as summarized in the inset of Fig. 1(c). Since the slope is directly correlated with the size of the gap, this implies that the correlation gap is enhanced under an applied magnetic field.

The sheet resistance $R_\square$ as a function of the gate voltage is summarized in Fig. 1(d). The resistance was $\sim$1 MΩ at the CNP and decreased to 1 kΩ when gate voltage was tuned to be 20 V away, yielding a large on-off ratio of $\sim$1000. Note that the largest measured sheet resistance $\sim$1 MΩ is much smaller than the insulation resistance ($\sim$10 GΩ) of our low-pass filters, indicating that the detected signals arise from the sample instead of from any leakage currents. The high-resistance region is highlighted by the blue shaded region in the figure, which covers a gate range $\sim$4.4 V. This gate variation can be translated to a carrier density variation $\sim 3.3\times10^{11}/\text{cm}^2$, which is very close to the number of VRH states per unit area in our samples. Given the band structure gap is $\sim$20 meV, as estimated from tight-binding calculations [15,25], this carrier density translates into a VRH DOS of $\sim 1.6\times10^{10}/(\text{meV cm}^2)$.

IV. DOS MODEL AND THE VRH CONDUCTION CHANNEL

To explain the observed T^{-1} dependence as well as the nonlinear I-V behavior, we propose that there is a hard gap in the VRH DOS centered around the Fermi level with a magnitude of $2k_BT_1$, where k_B is the Boltzmann constant. This is shown schematically in Fig. 2(a). There is also a small DOS bump at the CNP (center of the gap) that can give rise to a conduction channel parallel to the thermally activated/VRH conduction. It originates from the power-law delocalized tail of the states at the CNP, Anderson localized by weak random scatterings. Here, T_1 should be $\sim$10 K, as expected from the slope of the Arrhenius plots; this hard gap is one order of magnitude smaller than the band structure gap $2\Delta = 20$ meV estimated by the tight-binding calculations [15,25]. In the upper right inset of Fig. 2(b), it is shown that

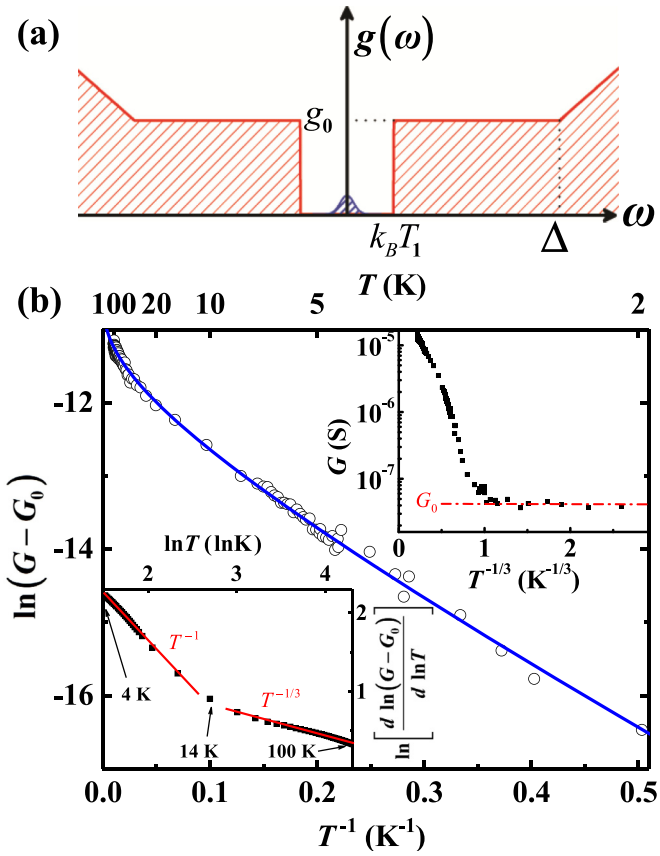

FIG. 2. Proposed density of states (DOS) model and temperature-dependent transport. (a) A schematic figure of the model DOS distribution. A hard gap $2k_BT_1$ in the variable-range hopping (VRH) states opens around the Fermi level, where the correlation gap k_BT_1 is much smaller than the band structure gap Δ. A small DOS bump at the center of the gap [charge neutrality point (CNP)] signifies the parallel conduction channel that arises from the Anderson-localized states. (b) $\ln(G-G_0)$ is plotted as a function of T^{-1}. Open circles are measured data, and blue line is the prediction of the proposed DOS model. The top right inset gives the raw conductance data plotted as a function of $T^{-1/3}$. A saturating temperature-independent parallel channel G_0 is clearly seen at $T<1$ K, as indicated by the red dashed curve. The bottom left inset is $\ln[d\ln(G-G_0)/d\ln(T)]$ plotted as a function of $\ln(T)$, where a crossover from T^{-1} to $T^{-1/3}$ is seen as shown by the fitted red straight lines.

the conductance saturates at G_0 when $T<1$ K. It should be emphasized that the conductance measured at low temperature is that from the sample instead of any leakage current of the measurement system. This point is confirmed by the observation of the dependence of the low-temperature conductance on both sample length and magnetic field. In other words, we have confirmed that the measured CNP resistance scales with the corresponding electrode separations shown in Fig. 1(a). This temperature-independent conductance channel is the manifestation of the spatial tunneling between the Anderson-localized states around the CNP. As temperature increases, the parallel VRH channel dominates. To demonstrate the temperature dependence, $\ln[d\ln(G-G_0)/d\ln(T)]$ is plotted as a function of $\ln(T)$ [32,38], as shown in the lower left inset of Fig. 2(b). The numerical derivative is obtained based on raw data smoothed by a Gaussian filter. The temperature dependence clearly exhibits a crossover at 14 K, from the thermal activation T^{-1} behavior to the VRH behavior with a constant DOS [39], i.e., $T^{-1/3}$. It should be noted that the crossover from T^{-1} to $T^{-1/2}$ and $T^{-1/4}$ has been reported in other thin-film three-dimensional (3D) systems, as discussed in Refs. [32,37]. Here, in our 2D antidot graphene system, only the T^{-1} to $T^{-1/3}$ crossover is observed, consistent with the fact that our system is 2D.

With this proposed DOS model [Fig. 2(a)], we apply the VRH mechanism to evaluate the conductance behavior. The VRH conductance is given by $\sigma=\sigma_0\exp(-R)$, where R is the spatial and energy range defined as [40,41]

$$R=\frac{x}{l}+\frac{\omega}{k_BT}, \tag{1}$$

where x/l describes spatial tunneling, with x being the spatial distance and l the effective size of the localized wave functions; ω/k_BT describes the thermal activation, with ω being the energy difference between the initial and final states. The temperature-dependent conductance, based on the DOS model, is given by [27]

$$\ln(G-G_0)=C-\frac{T_1}{T}-\left(\frac{3}{\pi g_0 l^2 k_BT}\right)^{1/3}, \tag{2}$$

where $G-G_0$ is the subtracted conductance, and g_0 is the constant VRH DOS beyond the gap. Equation (2) predicts a crossover between $T^{-1/3}$ and T^{-1} dependence that perfectly fits our experimental data, as shown in Fig. 2(b). The fitting yields $T_1=7$ K and $g_0k_Bl^2=0.03$ K^{-1}. Based on the Einstein relation and the room-temperature conductance of graphene, it is estimated that g_0 is $\sim1\times10^{10}/(\text{meV cm}^2)$, which is close to the value reported previously [22] and also on the same order as what we estimated above. It follows that the localization length l for the VRH states is $\sim$66 nm for the VRH states. It should be noted that the parameter g_0l^2 should remain invariant [22], owing to the fact that the average separation r_{ij} is always comparable with l while the DOS g_0 is proportional to r_{ij}^{-2}. It follows that g_0l^2 should be a constant to the first order approximation. We fix $g_0k_Bl^2=0.03$ K^{-1} and obtain the hard gap T_1 as a function of the magnetic field. The results are summarized in Fig. 3(a), shown by the black squares.

The increase in the gap size with increased magnetic field has been reported previously [23], but here, our gap size is smaller, and the magnetic field dependence is much weaker. If we attribute the gap variation to the Zeeman energy coupled to the spin, then the linear fitting of the dependence of the gap on the magnetic field will yield a g factor $\sim$1.6, close to the in-plane g factor reported in twisted double bilayer graphene [36]. Here, the gap enhancement under a perpendicular magnetic field can be either due to a spin polarized ground state [36] or the increase of Landau level energy separations [23]. A brief discussion about the magnetic field dependence of the gap variations is given in the SM [27]; however, the microscopic mechanism of the enhancement remains a topic to be further investigated.

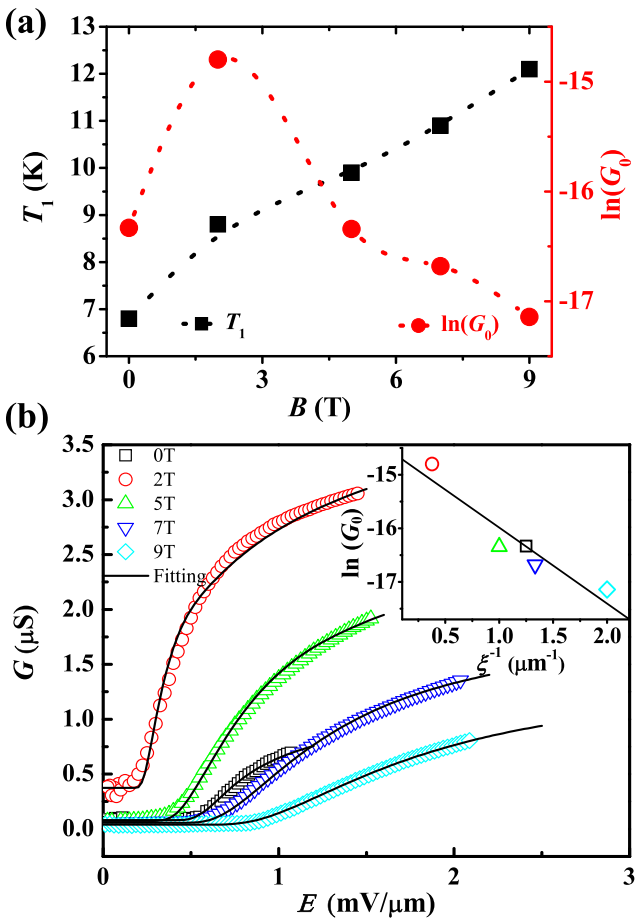

FIG. 3. Electric-field-dependent transport under different magnetic fields. (a) The hard gap T_1 (black squares) and conductance G_0 (red circles) are plotted as a function of the magnetic field. Dotted curves serve as a guide to the eye. (b) Conductance G is plotted as a function of electric field. Different colored symbols represent G measured at different applied magnetic field. Black curves are the theory predictions obtained by the proposed density of states (DOS) model [using Eq. (3)] with a hard gap as shown in Fig. 2(a). The inset shows the linear relation between the inverse of fitted localization length ξ and the plateau conductance G_0 observed at low temperatures. All data were measured at $T = 100$ mK.

V. TUNNELING CONDUCTION CHANNEL WITH ANDERSON-LOCALIZED STATES

At extremely low temperatures (much lower than T_1), the hopping/thermal activation conductance diminishes in magnitude, and the temperature-independent parallel channel becomes dominant. This temperature-independent channel was reported previously in different gapped graphene systems, such as graphene aligned to h-BN [7,9] and antidot graphene [22,25]. Here, we show this temperature-independent channel to be related to the Anderson-localized states in antidot graphene.

There is strong evidence that the VRH states originate from the quasiflat band/defect states inside the band structure gap of antidot graphene, as their corresponding carrier densities are very close to each other. By analyzing the wave function amplitudes of the simulated quasiflat band states (shown below), we find the Anderson-localized states also to result from these quasiflat band states since they have naturally (power-law) delocalized decaying tails that can contribute to the tunneling conduction at low temperatures. However, the VRH states and Anderson-localized states are very different in their DOS as well as in their localization length. This difference can be explained as follows.

Due to the correlation effect, the formation of a quasigap or a hard gap implies a low DOS, if not a zero DOS, at the Fermi level. The lack of states in the neighboring energy regions implies that the inelastic scatterings must be suppressed at low temperatures, owing to the lack of final states to realize such an inelastic process. That leaves multiple elastic scatterings that can lead directly to Anderson localization. Hence, the low DOS of the Anderson-localized states itself is evidence for the strong correlation effect in antidot graphene. Suppression of inelastic scatterings also means that, at low temperatures, where the accessible DOS is very low, conduction can only be by tunneling between the Anderson-localized states. In contrast, when the temperature increases, the charge carriers can access a much higher DOS with available states to enable inelastic phonon-assisted scatterings, which is part of the VRH conduction mechanism. A direct consequence is that the short localization length of the VRH states is determined by the inelastic scattering cutoff rather than by the coherent backscattering effect of Anderson localization that is due to multiple elastic scatterings. Hence, it is expected that the VRH states can hop from one hole edge to a nearby hole edge with a distance ∼50 nm. This is indeed close to our experimentally estimated VRH localization length (∼66 nm). Hence, the localization length of the VRH states is on the order of the separation between neighboring hole edges, i.e., after one inelastic scattering with the defect state of the neighboring hole edge, the state is localized by losing its phase coherence.

In Fig. 3(a), the tunneling conductance G_0 under different magnetic fields is shown by the red circles, where G_0 peaks at 2 T and then decreases as the magnetic field further increases. We attribute this G_0 variation to the change in the Anderson-localization length that underlies this parallel conductance channel. However, it is a bit surprising to see the nonmonotonic magnetoresistance effect associated with increasing magnetic field. The increase in the Anderson-localization length in the low magnetic field regime may be attributed to the negative magnetoresistance in the localization regime (see Fig. S5(b) in the SM [27]); however, the decrease in G_0, corresponding to a decrease in the localization length, is not yet understood. In fact, since G_0 is the spatial tunneling channel, it can be expressed as $G_0 \sim \exp(-r_{ij}/\xi)$, where r_{ij} is the spatial separation between two localized wave functions, and ξ is the Anderson-localization length. It should be noted that, despite the nonmonotonic behavior of the localization length as a function of the magnetic field, the $G_0 \sim \exp(-r_{ij}/\xi)$ behavior is still well followed, as seen in the inset to Fig. 3(b). A value of $r_{ij} = 1.4$ μm is obtained from the slope of the linear fit to $\ln(G_0)$ vs ξ^{-1}. The Anderson-localization length ξ, on the other hand, can be obtained from the electric field dependence of the conductance at 100 mK (see below); it has the value ranging from 0.5 μm at 9 T to the peak value of 2.6 μm at 2 T. The micron-scale localization length is in good consistency

with that reported previously [22]. Here, the increase in the Anderson-localization length can be attributed to the phase breaking of the coherent backscattering loop pairs, while the decrease of ξ for magnetic field >2 T can be interpreted as indicating a wave function shrinkage. However, a detailed explanation of the nonmonotonic behavior of the localization length is the task of future studies.

In the presence of an electric field, the carriers can accelerate under an applied electric field within the dephasing length to overcome the gap T_1. In this manner, the midgap states can access the VRH sites even at low temperature. Here, we show that the electric field dependence can be understood on a unified basis with the information obtained from the temperature variation of G.

In Fig. 3(b), we summarize the conductance at CNP as a function of electric field measured under different magnetic fields at $T = 100$ mK. We can see that all data show similar behavior, i.e., there is a low-conductance plateau at low bias, and with increasing field, the conductance increases dramatically when the field exceeds a critical value. This behavior can be modeled by VRH with an applied electric field; Eq. (1) is modified by inserting an electric field term [40,41] as follows:

$$R = \frac{x}{\xi} + \frac{\omega - eE\cos(\theta)\min(x, l_\varphi)}{k_B T}, \tag{3}$$

where E is the electric field, θ is the angle between electric field direction and hopping vector $\boldsymbol{x}$, min takes the minimum value between x and the dephasing length l_φ, the distance within which the carriers can accelerate to gain kinetic energy. Beyond the l_φ, the hot carriers lose the extra energy due to inelastic electron scatterings. The heating power due to the applied electric field is found to be on the order of 10^{-10} W, which is negligible as compared with the dilution refrigerator cooling power 460 μW.

Equation (3) establishes a connection between conductance $\sigma = \sigma_0 \exp(-R)$ and the electric field E. We use the relation $G(E) = G_0 + G_1 \exp(-R)$ to fit the electric field dependence of G, with G_0 being the plateau conductance and G_1 a constant. Parameters g_0 and T_1 of the proposed DOS model are obtained from temperature-dependence fittings of zero-bias $G(T)$, leaving three parameters G_1, ξ, and l_φ. For all the G vs E curves measured at different magnetic fields, we scan ξ from 100 nm to 4 μm and l_φ from ξ to 10ξ. By minimizing the error between the fitting curves and experimental data, (ξ, l_φ) can be accurately determined. Details are given in the SM [27].

The fitting results are shown by the black curves in Fig. 3(b); they are seen to agree very well with the experimental data under various applied magnetic field. Moreover, for different magnetic fields, the fittings give different values of ξ; the fitted localization length $1/\xi$ scales well with $\ln(G_0)$ as shown in the inset of Fig. 3(b). From the slope of 1.4 μm, we obtain an average area density of the Anderson-localized states on the order of $1/(1.4\ \mu\text{m})^2$, i.e., $5\times10^7/\text{cm}^2$. Therefore, at CNP of antidot graphene, it is expected that there are electrons and holes with an average spatial separation $\sim$1.4 μm at the Fermi level. It seems that, inside the correlation gap of the VRH states, the Anderson-localized electrons and holes can form a correlation energy ground state. A simple back-of-the-envelope estimate of the electron-hole correlation energy is $\sim e^2/(4\pi\varepsilon r_{ij}) \sim 0.4$ meV, which is on the same order of the observed correlation gap of VRH states. This observation is intriguing and requires further theoretical investigation.

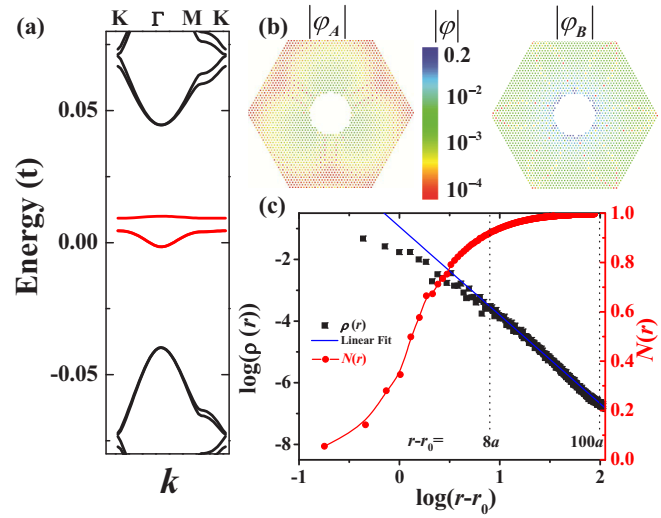

FIG. 4. Tight-binding simulated quasiflat band and wave functions of antidot graphene. (a) Tight-binding simulated band structure of antidot graphene with red curve being the quasiflat bands inside the band structure gap. (b) The wave function for the quasiflat bands at sublattices A and B. (c) Log-log plot of the wave function density ρ as a function of $r - r_0$, as shown by the black squares. The blue line is the linear fitting. Red circles denote the total wave function density within the distance r, i.e., $N(r)$ as a function of $r - r_0$. The red curve serves as a guide to the eye.

VI. TIGHT-BINDING SIMULATIONS OF ANTIDOT GRAPHENE

The origin of the Anderson-localized wave functions is previously unknown; here, we propose that it originates from the quasiflat bands in the close vicinity of the CNP. In the tight-binding simulations, the unit cell we used is a hexagon with a circular hole in the middle. We set the periodicity of the antidot lattice to be $L = 13$ nm and the average hole radius $r_0 = 1.8$ nm. Randomness is introduced by considering the angular-dependent radius $r(\theta)$ [27]. The simulated band structure is shown in Fig. 4(a). Apart from the regular gapped band structure for antidot graphene (black curves), there are quasiflat bands (red curves) inside the band structure gap. Here, we have selectively shown a few of them. The quasiflat bands are related to the local imbalance between two sublattices A and B [18,42]. They represent the defect states inside the band structure gap, hence different from the quasiflat bands observed in twisted bilayer graphene system [35,36]. The number of the quasiflat band states in the unit cell of experimental samples can be estimated by $\sqrt{\pi d/\sqrt{3}a} = 36$ [18], where $d = 100$ nm, and $a = 0.142$ nm is the carbon-carbon distance. It follows that the density is $36/S = 3\times10^{11}/\text{cm}^2$ where S is the area of the unit cell. This density is very close to the density of the shaded region in Fig. 1(d), implying that the high-resistance region around CNP must have originated from the quasiflat band states.

A typical simulated wave function for the quasiflat band around CNP is plotted in Fig. 4(b); the different magnitudes of the wave functions at sublattices A and B are related to the local imbalance between two sublattices [18,42]. The wave function exhibits a peak located near the edge of the hole. We calculate the total wave function within a radius r, i.e., $N(r) = \sum_{|r'|<r} |\varphi(r')|^2$ and wave function density $\rho(r) = dN(r)/dr/2\pi r$; they are shown in Fig. 4(c) by the red circles and black squares, respectively. While 90% of the wave functions are located near the edge ($|r - r_0| < 8a$), the wave functions decay in a power-law fashion away from the edge, as seen from the linear relation between log $\rho(r)$ and $\log(r - r_0)$. With different randomness, the power-law decay $\rho(r) \sim (r - r_0)^{-\beta}$ behavior is repeated with β varying from 1.5 to 4. These delocalized wave function tails can contribute to the low-temperature tunneling conduction, e.g., at T <1 K [see Fig. 2(b)]. As the carrier density of Anderson-localized states is $\sim 5\times10^7/\mathrm{cm}^2$, we can estimate the DOS of these tunneling wave functions by assuming the relevant energy range to be ~0.1 meV (~1 K). It follows that the DOS of the Anderson-localized states is $\sim5\times10^8/(\mathrm{meV\ cm}^2)$, which is on the same order as the value previously reported [22] and more than one order of magnitude smaller than the DOS of the VRH states.

VII. CONCLUSIONS

To recapitulate, the measured temperature- and electric-field-dependent conductance in antidot graphene can be well explained by the VRH mechanism together with the hard gap DOS model, attendant with a parallel conduction channel that comprises the states in the close vicinity of the CNP that are Anderson localized from the power-law delocalized wave function tails. The latter can be quantitatively understood within the tight-binding simulations. The fitted localization length is consistent with the parallel tunneling conductance at low temperatures. However, both the hard gap size enhancement under a magnetic field and the nonmonotonic magnetic field dependence of the localization length remain to be addressed in future investigations. Nevertheless, our experimental results suggest that, even inside a hard correlation gap, there can still be a coherence network that spans over the sample at ultralow temperatures, which might be observed in a tunneling spectroscopy setup as that shown in Ref. [43].

ACKNOWLEDGMENTS

P.S. wishes to acknowledge the support of Research Grants Council of Hong Kong, Grants No. 16304314 and No. 16308216. J.J.L. acknowledges the support of Taiwan Ministry of Science and Technology through Grants No. MOST 106-2112-M-009-007-MY4 and No. 110-2634-F-009-026, and the Center for Emergent Functional Matter Science of National Yang Ming Chiao Tung University from the Featured Areas Research Center Program within the framework of the Higher Education Sprout Project by the Ministry of Education (MOE) in Taiwan.

[1] K. S. Novoselov, A. K. Geim, S. V. Morozov, D. Jiang, Y. Zhang, S. V. Dubonos, I. V. Grigorieva, and A. A. Firsov, Science **306**, 666 (2004).
[2] K. S. Novoselov, A. K. Geim, S. V. Morozov, D. Jiang, M. I. Katsnelson, I. V. Grigorieva, S. V. Dubonos, and A. A. Firsov, Nature **438**, 197 (2005).
[3] Y. B. Zhang, Y. W. Tan, H. L. Stormer, and P. Kim, Nature **438**, 201 (2005).
[4] A. H. Castro Neto, F. Guinea, N. M. R. Peres, K. S. Novoselov, and A. K. Geim, Rev. Mod. Phys. **81**, 109 (2009).
[5] S. D. Sarma, S. Adam, E. H. Hwang, and E. Rossi, Rev. Mod. Phys. **83**, 407 (2011).
[6] B. Hunt, J. D. Sanchez-Yamagishi, A. F. Young, M. Yankowitz, B. J. LeRoy, K. Watanabe, T. Taniguchi, P. Moon, M. Koshino, P. Jarillo-Herrero, and R. C. Ashoori, Science **340**, 1427 (2013).
[7] L. A. Ponomarenko, R. V. Gorbachev, G. L. Yu, D. C. Elias, R. Jalil, A. A. Patel, A. Mishchenko, A. S. Mayorov, C. R. Woods, J. R. Wallbank, M. Mucha-Kruczynski, B. A. Piot, M. Potemski, I. V. Grigorieva, K. S. Novoselov, F. Guinea, V. I. Fal'ko, and A. K. Geim, Nature **497**, 594 (2013).
[8] C. R. Woods *et al.*, Nat. Phys. **10**, 451 (2014).
[9] R. V. Gorbachev, J. C. W. Song, G. L. Yu, A. V. Kretinin, F. Withers, Y. Cao, A. Mishchenko, I. V. Grigorieva, K. S. Novoselov, L. S. Levitov, and A. K. Geim, Science **346**, 448 (2014).
[10] Y. W. Son, M. L. Cohen, and S. G. Louie, Nature **444**, 347 (2006).
[11] Y.-W. Son, M. L. Cohen, and S. G. Louie, Phys. Rev. Lett. **97**, 216803 (2006).
[12] M. Y. Han, B. Özyilmaz, Y. Zhang, and P. Kim, Phys. Rev. Lett. **98**, 206805 (2007).
[13] X. Li, X. Wang, L. Zhang, S. Lee, and H. Dai, Science **319**, 1229 (2008).
[14] X. Wang, Y. Ouyang, X. Li, H. Wang, J. Guo, and H. Dai, Phys. Rev. Lett. **100**, 206803 (2008).
[15] T. G. Pedersen, C. Flindt, J. Pedersen, N. A. Mortensen, A.-P. Jauho, and K. Pedersen, Phys. Rev. Lett. **100**, 136804 (2008).
[16] J. A. Fürst, J. G. Pedersen, C. Flindt, N. A. Mortensen, M. Brandbyge, T. G. Pedersen, and A. P. Jauho, New J. Phys. **11**, 095020 (2009).
[17] J. Eroms and D. Weiss, New J. Phys. **11**, 095021 (2009).
[18] M. Vanević, V. M. Stojanović, and M. Kindermann, Phys. Rev. B **80**, 045410 (2009).
[19] M. Kim, N. S. Safron, E. Han, M. S. Arnold, and P. Gopalan, Nano. Lett. **10**, 1125 (2010).
[20] A. J. M. Giesbers, E. C. Peters, M. Burghard, and K. Kern, Phys. Rev. B **86**, 045445 (2012).
[21] E. C. Peters, A. J. M. Giesbers, and M. Burghard, Phys. Status Solidi B **249**, 2522 (2012).
[22] H. Zhang, J. Lu, W. Shi, Z. Wang, T. Zhang, M. Sun, Y. Zheng, Q. Chen, N. Wang, J.-J. Lin, and P. Sheng, Phys. Rev. Lett. **110**, 066805 (2013).
[23] E. C. Peters, A. J. M. Giesbers, U. Zeitler, M. Burghard, and K. Kern, Phys. Rev. B **87**, 201403(R) (2013).

[24] A. Sandner, T. Preis, C. Schell, P. Giudici, K. Watanabe, T. Taniguchi, D. Weiss, and J. Eroms, Nano. Lett. **15**, 8402 (2015).
[25] J. Pan, T. Zhang, H. Zhang, B. Zhang, Z. Dong, and P. Sheng, Phys. Rev. X **7**, 031043 (2017).
[26] B. S. Jessen, L. Gammelgaard, M. R. Thomsen, D. M. A. Mackenzie, J. D. Thomsen, J. M. Caridad, E. Duegaard, K. Watanabe, T. Taniguchi, T. J. Booth, T. G. Pedersen, A.-P. Jauho, and P. Bøggild, Nat. Nanotech. **14**, 340 (2019).
[27] See Supplemental Material at http://link.aps.org/supplemental/10.1103/PhysRevB.103.235114 for (i) estimation of r_S in antidot graphene, (ii) extended discussion on temperature dependence of conductance, (iii) temperature dependence of conductance with a hard gap, (iv) magnetic field dependence of hard gap, (v) extraction of parameter values from the electric field dependence of conductance, and (vi) tight binding simulations of antidot graphene.
[28] R. Chicon, M. Ortũno, and M. Pollak, Phys. Rev. B **37**, 10520 (1988).
[29] E. H. Hwang and S. Das Sarma, Phys. Rev. B **75**, 205418 (2007).
[30] P. Dai, Y. Zhang, and M. P. Sarachik, Phys. Rev. Lett. **69**, 1804 (1992).
[31] I. Terry, T. Penney, S. von Molnár, and P. Becla, Phys. Rev. Lett. **69**, 1800 (1992).
[32] J.-J. Kim and H. J. Lee, Phys. Rev. Lett. **70**, 2798 (1993).
[33] E. Bielejec, J. Ruan, and W. Wu, Phys. Rev. Lett. **87**, 036801 (2001).
[34] Y. Nam, D.-K. Ki, D. Soler-Delgado, and A. F. Morpurgo, Science **362**, 324 (2018).
[35] Y. Cao, V. Fatemi, A. Demir, S. Fang, S. L. Tomarken, J. Y. Luo, J. D. Sanchez-Yamagishi, K. Watanabe, T. Taniguchi, E. Kaxiras, R. C. Ashoori, and P. Jarillo-Herrero, Nature **556**, 80 (2018).
[36] Y. Cao, D. Rodan-Legrain, O. Rubies-Bigorda, J. M. Park, K. Watanabe, T. Taniguchi, and P. Jarillo-Herrero, Nature **583**, 215 (2020).
[37] N. Marković, C. Christiansen, D. E. Grupp, A. M. Mack, G. Martinez-Arizala, and A. M. Goldman, Phys. Rev. B **62**, 2195 (2000).
[38] H. Vinzelberg, A. Heinrich, C. Gladun, and D. Elefant, Philos. Mag. B **65**, 651 (1992).
[39] N. F. Mott, J. Non-Cryst. Solids. **8–10**, 1 (1972).
[40] M. Singh, Y. Tarutani, U. Kabasawa, and K. Takagi, Phys. Rev. B **50**, 7007 (1994).
[41] M. Singh, R. B. Thompson, and O. Dumas, Phys. Rev. B **53**, 6806 (1996).
[42] M. Inui, S. A. Trugman, and E. Abrahams, Phys. Rev. B **49**, 3190 (1994).
[43] J. Martin, N. Akerman, G. Ulbricht, T. Lohmann, J. H. Smet, K. Von Klitzing, and A. Yacoby, Nat. Phys. **4**, 144 (2008).